Appl. Phys. A 89, 133–139 (2007)
DOI: 10.1007/s00339-007-4128-0
Applied Physics A
Materials Science & Processing

Rapid communication

A. SUBRAMANIAN[1]
T.-Y. CHOI[2]
L.X. DONG[1]
J. THARIAN[3]
U. SENNHAUSER[3]
D. POULIKAKOS[4]
B.J. NELSON[1,✉]

Local control of electric current driven shell etching of multiwalled carbon nanotubes

[1] Institute of Robotics and Intelligent Systems, ETH Zurich, 8092 Zurich, Switzerland
[2] Department of Mechanical and Energy Engineering, University of North Texas, Denton, TX 76203, USA
[3] Electronics/Metrology Laboratory, EMPA, 8600 Dubendorf, Switzerland
[4] Laboratory of Thermodynamics in Emerging Technologies, ETH Zurich, 8092 Zurich, Switzerland

Received: 8 January 2007/Accepted: 7 May 2007
Published online: 14 June 2007 •

ABSTRACT We report on a novel method for local control of shell engineering in multiwalled carbon nanotubes (MWNTs) using Joule-heating induced electric breakdown. By modulating the heat dissipation along a nanotube, we can confine its thinning and shell breakdown to occur within localized regions of peak temperatures, which are distributed over one-half of the NT length. The modulation is achieved by using suitably designed nanomachined heat sinks with different degrees of thermal coupling at different parts of a current-carrying nanotube. The location of electric breakdown occurs precisely at the regions of high temperatures predicted by the classical finite-element model of Joule heating in the MWNT. The experiments herein provide new insight into the electric breakdown mechanism and prove unambiguously that shell removal occurs due to thermal stress, underpinning the diffusive nature of MWNTs. The method demonstrated here has the potential to be a powerful tool in realizing MWNT bearings with complex architectures for use in integrated nanoelectromechanical systems (NEMS). In addition, the breakdown current and power in the nanotubes are significantly higher than those observed in nanotubes without heat removal via additional heat sinks. This indicates future avenues for enhancing the performance of MWNTs in electrical interconnect and nanoelectronic applications.

PACS 73.63.Fg; 65.80.+n

1 Introduction

Current driven electric breakdown of individual carbon shells [1–7] is a powerful method for modifying the as-synthesized closed cap nested shell structure of multiwalled carbon nanotubes (MWNTs). In this method, the thermal stress caused by Joule heating of current-carrying nanotubes is used to initiate defects in the nanotube structure and vaporize individual shells with an accompanied reduction in nanotube conductance. The capability of engineering nanotube geometry is expected to find applications in the next-generation of nanoelectromechanical systems. For instance, nanotube linear and rotary bearings [8–11] constructed by current driven breakdown can be used to realize nanoactuators [12–14], nanoswitches/memories [15–17] and GHz oscillators [18–21]. In addition, permanent modification of shell geometry has been demonstrated as a suitable technique to tailor electrical properties for nanoelectronic applications [1].

Precise control over breakdown location and NT shell architecture is an important requirement for these applications. In previous reports, shell structuring has been performed by connecting the nanotubes to metallic contacts at their distal ends and driving currents [1, 2, 4, 13, 15]. With the electrical and phonon transport through MWNTs being diffusive at length scales on the order of a hundred nanometers, Joule-heating induces peak temperatures at nanotube mid-lengths and results in the loss of carbon atoms in the outer shells of these regions between the contacting electrodes. However, with this simple two-electrode configuration, the temperature distribution along the nanotube will always result in shell breakdown at nanotube mid-lengths. Presently, we demonstrate a novel approach to precisely alter, control or restrict the region over which shell structuring occurs. This is achieved by modifying the heat dissipation along the length of a current-carrying nanotube in order to controllably create localized regions of high nanotube temperatures within which shell removal occurs.

2 Results

In our electric breakdown experiments, we employ MWNT nanostructures where the nanotube is sandwiched between two layers of metal at its distal ends. These metallic contacts at the distal ends serve as the biasing electrodes and by driving currents beyond the shell breakdown threshold, we etch the NT shells starting from the outermost and proceeding towards the inner ones. Because shell removal is driven by Joule-heating induced structural defects such as kinks or holes [3] and current transport through MWNTs at length scales of the order of a hundred nanometers is diffusive [3, 6], shell removal is centered about the mid-point of the suspended nanotubes. This is schematically illustrated in Fig. 1a and an SEM image of a shell structured nanotube is shown in Fig. 1b. This shell structure is similar to the thinning observed in previously

✉ Fax: +41-44-632-1078, E-mail: bnelson@ethz.ch

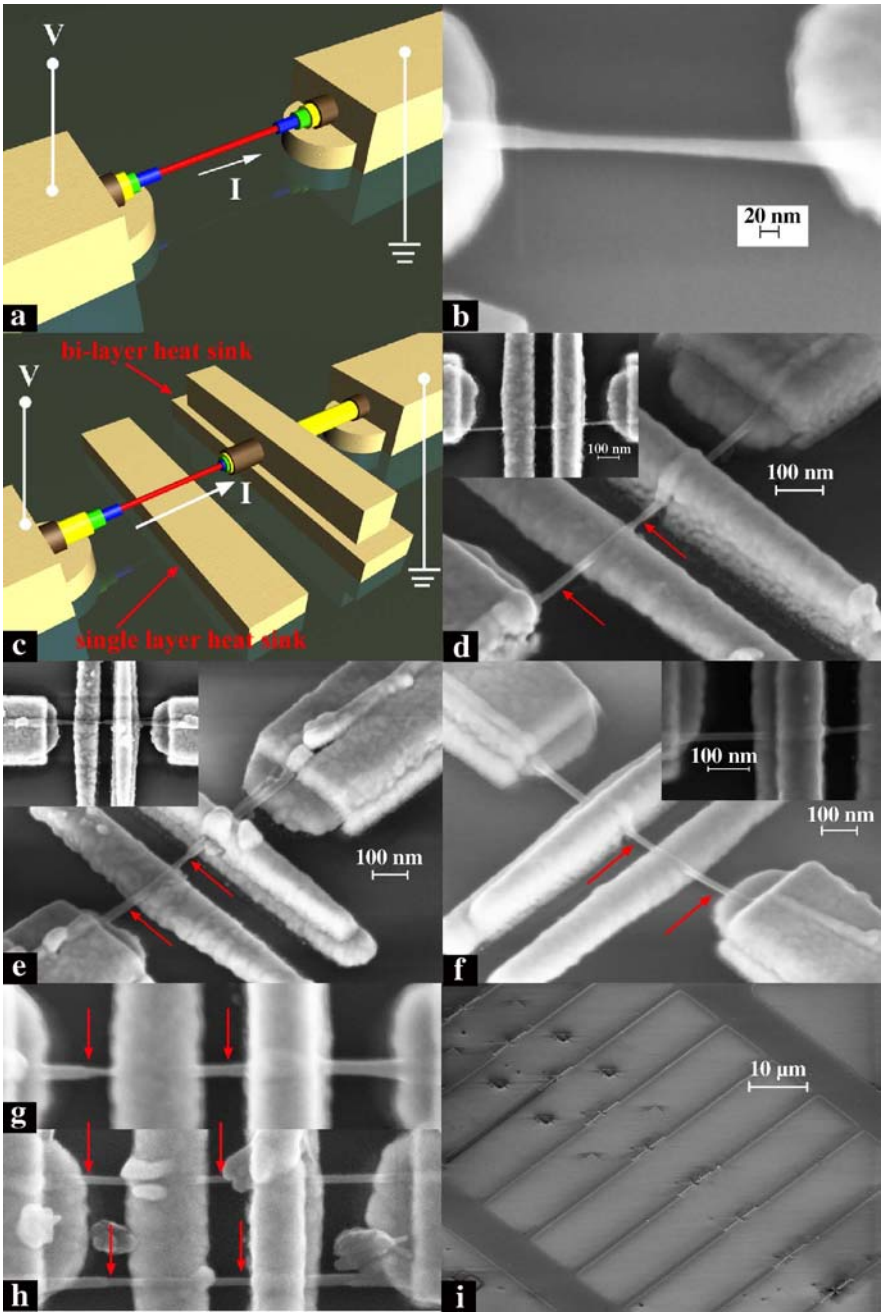

FIGURE 1 Shell engineering results with a comparison between shell architectures arising from different nanostructure designs. (**a**) Schematic illustration of a MWNT without metallic heat sinks. (**b**) SEM image of electric breakdown at NT mid-lengths in such nanostructures. (**c**) Illustration of a MWNT nanostructure with two additional heat sinks and its electrode wiring scheme. (**d–f**) SEM images of nanostructures, of the type shown in panel (**c**), after electric breakdown. It can be clearly seen that the thinning is predominantly confined to one half of the NTs (on the side containing the single-layer heat sink). The images are taken at a stage tilt of 40°. Images in inset of panels (**d**) and (**e**) show the top-view of the NTs. The inset in panel (**f**) shows the top-view of the heat sink region at a higher magnification so that the changes in NT diameter can be clearly seen. (**g–h**) SEM images of a few more NTs showing localized thinning. (**i**) Typical nanoelectrode array design

reported two-electrode current-driven breakdown experiments.

We find that we can controllably alter this mid-length electric breakdown in MWNTs and restrict its occurrence predominantly over one half of the NT by introducing additional, spatially separated metallic layers in contact with the current-carrying nanotube. Figure 1c illustrates a nanotube in contact with two additional metallic regions that are situated between the biasing electrodes. The additional metallic regions are held at a floating potential and serve as heat sinks that remove the Joule heat generated in NTs. One of these heat sinks is comprised of two layers of metal that sandwich the nanotube and has a contact area that is greater than at least half of the nanotube's surface area. The other heat sink has only one layer of metal underneath the NT and due to the cylindrical NT surface, makes only a line contact with the NT on top of it. Since the thermal contact resistance and removal of Joule heat generated in the NTs through these metallic contacts is dependant on the contact area, we find that heat dissipation is higher at the two-layer heat sink as compared to the single-layer heat sink. This results in a non-uniform temperature profile along the NT length with higher temperatures in the half of the NT that is in contact with the single layer heat sink. A direct consequence of such a temperature distribution is that the Joule heating induced electric breakdown occurs predominantly in this half of the NT. SEM images of nanotubes where such location-controlled thinning occurs are shown in Fig. 1d–h. In these images, substantial shell removal occurs in the region spanning the red arrowheads. It can be seen that the region of thinning is confined to only one half of the nanotube that is in contact with the single-layer heat sink. Further analysis of the length of thinning and its causes is provided in Sect. 3.3.

Another aspect of our method is its suitability for batch fabrication. The nanofabrication procedure employed to realize the nanostructures starts with the definition of lower electrodes and heat sinks (15 nm Cr/45 nm Au) on top of a silicon chip covered with an insulating 500 nm oxide film. This layer is defined using electron beam lithographic patterning of a bi-layer resist (of P(MAA)/PMMA), which is followed by metal deposition and lift-off. Next, MWNT arrays are assembled on the nanoelectrodes using composite-field dielectrophoresis [22, 23]. The top metal layer is then defined using electron beam lithography. Finally, the shell structuring of NTs is carried out using the electric breakdown technique in air and the results are investigated using SEM imaging. An image of the nanostructure array design in shown in Fig. 1i.

3 Discussion

3.1 *Thermal analysis*

In this sub-section, we present the results from finite-element simulations of the temperature distribution created in a current-carrying MWNT with a nanostructure of this type shown in Fig. 1c. This analysis focuses on the impact of the metallic heat sink design on heat removal from the nanotube and the resulting temperature distribution along its length.

Recent studies using electrostatic microscopy [24] and scanning thermal microscopy [25] revealed that MWNTs are diffusive heat conductors. Other studies showed the same classical nature by utilizing the 3-omega method [26, 27]. These studies provide insight on mesoscopic energy carrier transport in nanotubes, indicating that the classical approach is valid for obtaining the temperature distribution of the MWNTs subjected to Joule heating. Therefore, in this study we employed the classical finite element method using a commercial software package (CFD-ACE) to find the temperature distribution along a single MWNT that has the same configuration shown in Fig. 1c. For simplicity, the MWNT is modeled to have a 20 nm wide square cross-section without changing the physics of the problem. The thermal contact resistance between the NT and lower metal electrode is assumed to be 3×10^7 K/W, which is based on experimental results reported in [28]. A fictitious layer 4 nm thick is inserted at the contact, giving rise to a thermal resistance load. The ratio of the contact areas at the upper and lower layer is set at 10π by assuming the top half of the periphery of the NT is covered by the upper metal layer and the lower metal contact width is 1 nm (a line contact). The steady-state temperature profile and transient temperature evolution are shown in Fig. 2a–b. Contrary to the two electrode configuration (Fig. 1a), the profile shows an asymmetrical characteristic. This is due to an imbalance in the contact thermal load. The high temperature region in the central area coincides with the thinned pattern as shown in Fig. 1e–f. The temperature difference of about 200 K is large enough to induce defect formations in a selective manner at the critical (threshold) condition, which is strong evidence of the diffusive nature of MWNTs.

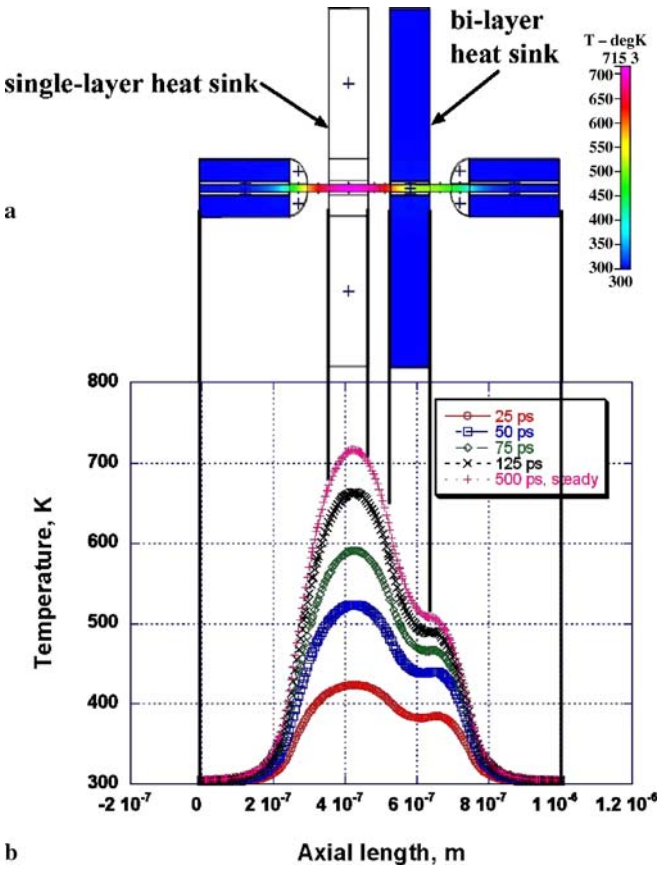

FIGURE 2 Impact of heat removal via additional heat sinks on the temperature distribution along a NT. (**a**) Contour plot of the steady state temperature distribution along the NT length computed using a finite-element heat transfer model. (**b**) The NT temperature as function of length is plotted at different time intervals after the application of the biasing current. It can be seen that the MWNT nanostructure attains thermal equilibrium for an applied external bias after approximately 500 ps. The black lines are shown to indicate the corresponding regions of the nanostructure in panel (**a**)

3.2 *Equivalent electrical circuit and Joule heat generation analysis*

In this section, we provide a qualitative analysis of the equivalent electrical circuit and Joule heat generation along the length of the MWNT nanostructure (Fig. 1c) used in our experiments. As a first step, we estimate the electrical contact resistance at the two biasing electrodes and the average resistivity of our MWNTs. This is obtained by measuring the circuit resistance across two arrays of MWNTs with different lengths between biasing electrodes in a two electrode configuration (of the type shown in Fig. 1a). The equivalent electrical circuit across a single MWNT bridging two electrodes is shown in Fig. 3a. In array 1, the length of the MWNT between biasing electrodes was 340 nm and the measured circuit resistance, at 1.50 V, across 10 nanotubes in parallel was 1.22 kΩ (1.50 V/1.23 mA). In array 2, the length of the MWNT between biasing electrodes was 240 nm and the measured electrical circuit resistance across 11 nanotubes in parallel was 1.00 kΩ (1.50 V/1.50 mA). The average resistance across a single nanotube, which is computed as the total array circuit resistance multiplied by the number of nanotubes in the array, can be expressed using the equation

$$R_{\text{ave}} = 2R_{\text{c,be}} + \frac{\varrho l}{A}\,, \tag{1}$$

where $R_{\text{c,be}}$, ϱ, l and A represent the average contact resistance at the biasing electrode, nanotube resistivity, length, and cross-sectional area, respectively. From the measured values of R_{ave} in arrays 1 and 2, we obtain $R_{\text{c,be}} \left(R_{\text{c,be}} = \frac{(R_{\text{ave},2} l_1 - R_{\text{ave},1} l_2)}{2(l_1 - l_2)}\right)$ to be

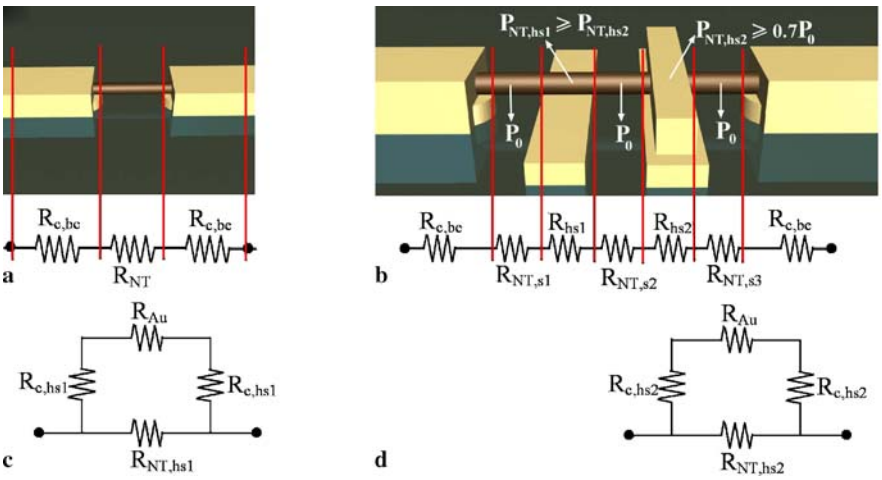

FIGURE 3 Electrical circuit and Joule heat generation analysis. (**a**) Equivalent electrical circuit across a NT suspended across two biasing electrodes. The nanostructure is shown on top while the corresponding circuit is shown in the bottom of this panel. (**b**) Equivalent electrical circuit across a NT which is connected to additional heat sinks separate from the biasing electrodes at its distal ends. In this image, the volumetric Joule heat generation (as a function of the value in suspended NT segments, P_0) is also indicated with *white arrows* at different segments of the nanotube. (**c–d**) Equivalent electrical circuit at the single and bi-layer heat sinks, respectively

4.1 kΩ. The nanotube cross-sectional area A is computed as $\pi(d_0^2 - d_i^2)/4$ using outer and inner diameter values of 20 and 4 nm, respectively. The nanotube resistivity ϱ can be further obtained to be 3.6 μΩ m. It is important to note that our measurements of MWNT resistivity lie within the range of values previously reported in [29, 30].

The nanostructure used for location controlled shell engineering consists of seven resistances in series, as shown in Fig. 3b, and the circuit resistance across such a nanostructure is given by

$$R_{\text{circuit}} = 2R_{\text{c,be}} + R_{\text{NT,s1}} + R_{\text{NT,s2}} + R_{\text{NT,s3}} + R_{\text{hs1}} + R_{\text{hs2}} \,, \qquad (2)$$

where $R_{\text{c,be}}$ represents the contact resistance at the two biasing electrodes, while $R_{\text{NT,s1}}$, $R_{\text{NT,s2}}$ and $R_{\text{NT,s3}}$ represent the intrinsic resistances of nanotube segments that are suspended in air (Fig. 3b). R_{hs1} and R_{hs2} denote the effective resistance offered by the single-layer and bi-layer heat sink regions, respectively. It is important to note that, with the nanotube source material and biasing electrode designs remaining the same, the average contact resistance at biasing electrodes and NT resistivity will be the same for nanostructures of the type shown in Fig. 3a and b.

Each of the metallic heat sink regions is comprised of the NT in parallel with the gold pads, as shown in Fig. 3c–d. From the resistivity value of 2.2 μΩ cm for gold, we compute the gold pad resistances to be ∼ 8.5 mΩ and 17 mΩ at the single and bi-layer heat sinks, respectively. Since this is several orders of magnitude lower than the contact resistances at heat sinks, it can be neglected. The NT currents at the single ($I_{\text{NT,hs1}}$) and bi-layer ($I_{\text{NT,hs2}}$) heat sinks can then be expressed in terms of the current in NT segments that are suspended in air (I_0) as

$$I_{\text{NT,hs1}} = \frac{2R_{\text{c,hs1}}}{2R_{\text{c,hs1}} + R_{\text{NT,hs1}}} I_0 \qquad (3)$$

$$I_{\text{NT,hs2}} = \frac{2R_{\text{c,hs2}}}{2R_{\text{c,hs2}} + R_{\text{NT,hs2}}} I_0 \,, \qquad (4)$$

where $R_{\text{c,hs1}}$ and $R_{\text{c,hs2}}$ denote the contact resistances at the single and bi-layer heat sinks respectively. $R_{\text{NT,hs1}}$ and $R_{\text{NT,hs2}}$ represent the intrinsic NT resistances in the single and bi-layer heat sinks, respectively. Even though the bi-layer heat sink has two layers of metal sandwiching the NT, the length of NT-metal contact at the bi-layer heat sink is much smaller than that at the biasing electrodes (NT overlap lengths at the biasing electrodes is ∼ 0.5 to 2 μm, while it is only 135 nm at the heat sinks). In addition, with only one layer of metal underneath the NT, the area of NT–metal contact in the single layer heat sink is smaller than that in the bi-layer heat sink. Since contact resistance increases with decreasing contact area [31], we can write

$$R_{\text{c,hs1}} \geq R_{\text{c,hs2}} \geq R_{\text{c,be}} = 4.1\,\text{k}\Omega \,. \qquad (5)$$

From (3–5) and by substituting the value of $R_{\text{NT,hs2}}$, which is computed using the known values for NT resistivity and length, we obtain

$$I_{\text{NT,hs1}} \geq I_{\text{NT,hs2}} \geq 0.84\, I_0 \,. \qquad (6)$$

It is important to note that the volumetric power generation, which is defined as the Joule heat generated per unit volume, is proportional to the square of the current. Thus, from (6), we can compute the volumetric power generation within the NTs in the single layer ($P_{\text{NT,hs1}}$) and bi-layer heat sinks ($P_{\text{NT,hs2}}$) as

$$P_{\text{NT,hs1}} \geq P_{\text{NT,hs2}} \geq 0.7\, P_0 \,. \qquad (7)$$

Equation (7) shows that the volumetric Joule heat generation within the NT in the single layer heat sink is more than that generated within the NT in the bi-layer heat sink. As a result, the half of the NT that lies in the bi-layer heat sink experiences less heat generation as compared to the other half which lies in the single layer heat sink. This non-uniform power generation within the nanotube is expected to further increase the temperature difference between the single and bi-layer segments beyond that computed in Fig. 2a–b, where it was assumed that the power density along the nanotube remained constant. This Joule heat distribution at different segments of the nanotube is also highlighted in Fig. 3b.

3.3 *Electrical measurements*

In this section, we present the electric breakdown measurements for engineering an array of 13 NTs with heat sinks as illustrated in Fig. 1c. For the shell structuring process, the primary objective is to remove at least 5 outer shells in each nanotube. This has been shown to provide structures suitable for operation as nanobearings with low friction [13] and also results in structures where the thinning is large enough to be observed with SEM imaging. We find that the threshold voltage for removing these outer shells in each NT of the array is spread over a range ($V_{\text{TH, min}}$ to $V_{\text{TH, max}}$), which we refer to as the 'array breakdown spectrum'.

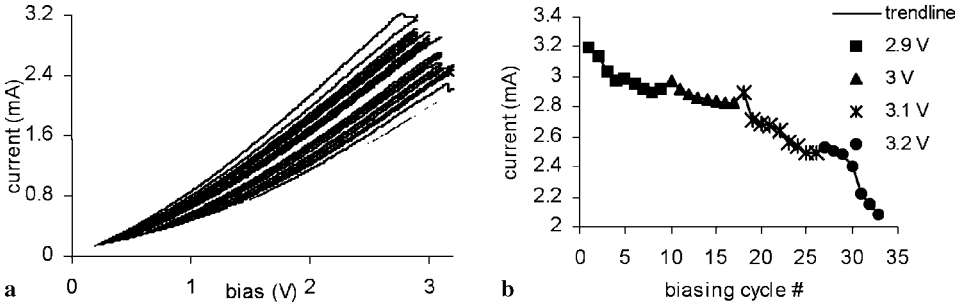

FIGURE 4 Electric breakdown measurements (**a**) I–V plots during the successive biasing cycles. The increasing threshold voltages required as the etching of shells progresses from the outermost to inner ones can be seen here. (**b**) The evolution of current I_0 (defined as current at V_{max} for each cycle in panel (**a**)) with successive biasing cycles can be seen in this plot. The voltage values given in the legend indicate the V_{max} value for that cycle

There are two reasons for this spread in breakdown voltages: the threshold voltage for vaporizing shells within a single nanotube increases from the outer to inner shells [31], and also the voltage for electric breakdown is likely to vary slightly from one NT to the other in the array due to possible variations in nanotube properties.

An important requirement for realizing partial thinning of NTs is to precisely determine this array breakdown spectrum. This is because, if the applied bias is far higher than the breakdown range, it results in a catastrophic breakdown of all NT shells in a single step. In order to prevent this failure mode, our biasing approach involves applying repeated voltage sweeps from 0 to V_{max}, where the starting value for V_{max} is very low (typically, 1.5 V). We refer to these individual sweeps from 0 to V_{max} as a 'biasing cycle' or simply 'cycle'. The shell removal in NTs is monitored using the current I_0, defined as the current at V_{max}, during successive cycles. We increase the value of V_{max} by 10 mV during subsequent cycles until the initiation of shell breakdown in the array. After the initiation of shell breakdown in the NT array, indicated by a reducing value of I_0 between successive cycles, we keep the value of V_{max} constant during successive cycles. After the removal of all shells corresponding to V_{max}, the value of I_0 is found to stabilize and we subsequently increase the value of V_{max} by 10 mV in the next cycle in order to remove the next set of inner shells with a higher breakdown threshold. This process is repeated until the value of I_0 in the last cycle is approximately 70% of I_0 before the initiation of breakdown in nanotubes. From more than 25 experiments involving electric breakdown in single NTs and NT arrays, we find that this is an appropriate termination point which results in the breakdown of at least five outer shells.

For the array of the 13 NTs under discussion, the breakdown spectrum was found to occur over the 2.9 to 3.2 V range and the shell engineering process required 33 biasing cycles. The I–V plots during these 33 cycles are shown in Fig. 4a. Reducing currents with successive cycles due to the vaporization of NT shells can be discerned from these plots. Another important attribute that can be observed in these plots is that the voltage required for removing the inner shells is higher than that for the outermost NT shells. The value of I_0 (defined as current at V_{max}), which is used to monitor the breakdown process, is shown as a function of the biasing cycles in Fig. 4b. It can be seen that I_0 decreases from 3.19 mA at the start of shell breakdown (in cycle # 1 with V_{max} of 2.9 V) to 2.08 mA at the termination of breakdown (in cycle # 33 with V_{max} of 3.2 V). We found that 11 of the 13 NTs in this array showed appreciable thinning, which was confined predominantly in the half-segment comprising the single layer heat sink. The breakdown in the remaining two NTs could not be discerned within the resolution limits of SEM imaging.

The electric breakdown measurements also provide important insights into the impact of Joule heat removal via metallic heat sinks on MWNT current transport and electric breakdown properties. Table 1 provides a comparison between two MWNT arrays. One array consists of 10 NTs with a structure similar to Fig. 1a where there are no heat sinks along the NT length. The second array involves 13 NTs with heat sinks along their lengths as shown Fig. 1c. It is important to note that this second array is the same as the one previously discussed in Fig. 4a–b. As listed in Table 1, the nanotubes in the array with heat sinks are longer than those in the array without heat sinks (620 nm vs. 340 nm). In the absence of heat sinks, the nanotubes can be considered as cylindrical elements with heat dissipation occurring primarily via contacts at their ends. In this case, the Joule heating temperature (T) will be directly proportional to both the power generated (P) and the nanotube length (L). With the nanotube resistance and power being proportional to its length, T will vary as L^2. Hence, for the same current levels, Joule heating is expected to increase with increasing nanotube lengths. Since shell structuring is caused primarily by Joule heating, both the threshold breakdown current and power are expected to decrease with increasing lengths. This argument is also supported by the previous modeling and experimental results reported in [5, 32, 33].

However, we find that the average shell breakdown current and power are higher for the array with longer nanotubes as compared to those for the ar-

Array configuration	Two biasing contacts, no heat sinks (Fig. 1a)	Two biasing contacts, two heat sinks (Fig. 1c)
No. of nanotubes (n)	10	13
Length of nanotubes (L)	340 nm	620 nm
Breakdown spectrum ($V_{TH,\,min}$ to $V_{TH,\,max}$)	2.3 to 2.4 V	2.9 V to 3.2 V
Average breakdown current ($I_{TH,\,ave} = I_{TH}/n$)	192.8 μA (1.92 mA/10)	245 μA (3.19 mA/13)
Breakdown power ($I^2_{TH,\,ave}R_{ave}$)	150.7 μW	384.4 μW

TABLE 1 Comparison of current transport and electric breakdown between MWNT nanostructures with and without heat removal via metallic heat sinks

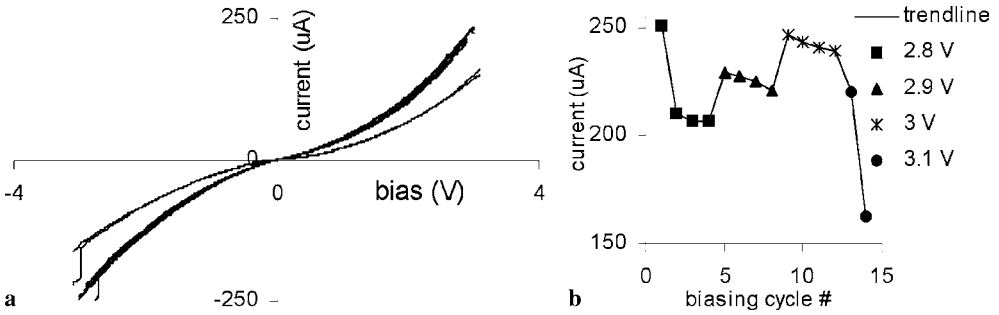

FIGURE 5 Electric breakdown measurements for a single NT device. (**a**) *I–V* plots during the successive biasing cycles. (**b**) The evolution of current I_0 (defined as current at $-V_{max}$ for each cycle in panel (**a**)) with successive biasing cycles can be seen in this plot. The voltage values given in the legend indicate the V_{max} value for that cycle

ray with shorter nanotubes. For the array with 340 nm long NTs, the average breakdown current and power were observed to be 192 μA and 150 μW, respectively. In the case of the second array with 620 nm NTs, the average breakdown current increases by 22% (to 245 μA), while the power capacity is enhanced by 156% (to 384 μW). We believe that this improvement in MWNT current transport and power capacities is caused by the enhanced Joule heat removal in nanostructures with additional heat sinks. Thus, these results unambiguously prove that electric breakdown in MWNTs is caused by thermal stresses and can be pushed to a higher threshold by effective removal of Joule heat generated in current carrying nanotubes. This mechanism is expected to provide efficiencies in the performance of MWNTs for electrical interconnect and nanoelectronics applications.

Finally, it is interesting to note the length of the nanotube over which thinning occurs in our nanostructures. In most nanotubes, the outermost shells are removed over a region that starts in the segment between the two heat sinks and terminates near the biasing electrode that is close to the single layer heat sink. This structure is schematically illustrated in Fig. 1c and can also be seen in the SEM images of Fig. 1e. However, in a few NTs, we find that, though the thinning occurs predominantly over the single-layer heat sink half of the nanotube, the nanotube thinning directly on top of the single layer heat sink is lower than that in the regions that are suspended in air (Fig. 1d). We believe that this is caused by the increased contact area between the NT and the single-layer heat sink (due to local deformation of the tube by van der Waals forces), resulting in lower electrical and thermal contact resistances. This will result in lower Joule heat generation in the nanotube directly over the single-layer heat sink and reduce temperatures as well as shell removal as compared to the segments suspended in air.

4 Conclusion

We have presented a novel approach for local control of electric breakdown in MWNTs. Precise control over the shell removal location is achieved by using suitably designed metallic heat sinks with different degrees of coupling to the current carrying nanotube. This is an important capability that will find applications in nanotube shell engineering for use as nanobearings in the next generation of nanoelectromechanical systems. The demonstration of this nanofabrication technique with arrays of MWNTs and its suitability for integration with conventional silicon micro/nanomachining processes further enhances the significance of these results. Another attribute of these structures is the significant improvements in MWNT current and power carrying capacity achieved by efficient Joule heat dissipation. These are important metrics that are expected to have an impact on the use of MWNTs for electrical interconnect and nanoelectronic applications.

ACKNOWLEDGEMENTS The authors thank Dr. H. Sehr and the clean room staff of the laboratory for micro and nanotechnology at the Paul Scherrer Institute (PSI), Villigen, Switzerland for providing oxidized silicon wafers that were used as substrates in the experiments.

Appendix: Electric breakdown measurements for a single device

In this section, we provide the electric breakdown measurements for a single MWNT nanostructure with heat sinks as illustrated in Fig. 1c of the main text. In this experiment, we sweep the voltage from $-V_{max}$ to $+V_{max}$ in 10 mV increments and 100 μs time-steps in a 'biasing cycle'. For each cycle, I_0 is defined as the magnitude of current at $-V_{max}$. For each V_{max}, the biasing cycle is repeated several times until there is no further shell breakdown at that voltage. For the nanotube in this experiment, shell breakdown was initiated at 2.8 V and we repeated the biasing cycles until the value of I_0 was approximately 70% of I_0 before the initiation of breakdown. Assuming the biasing electrode contact resistance to be the same as the average value computed in Sect. 3.2 (which is justified since the nanotube source material and the biasing electrode designs remain the same), the NT breakdown power is computed to be 408.4 μW. The I-V plots during the engineering of this nanotube are shown in Fig. 5(a) and the evolution of current I_0 with the successive biasing cycles is shown in Fig. 5(b).

REFERENCES

1 P.G. Collins, M.S. Arnold, P. Avouris, Science **292**, 706 (2001)
2 P.G. Collins, M. Hersam, M. Arnold, R. Martel, P. Avouris, Phys. Rev. Lett. **86**, 3128 (2001)
3 J.Y. Huang, S. Chen, S.H. Jo, Z. Wang, D.X. Han, G. Chen, M.S. Dresselhaus, Z.F. Ren, Phys. Rev. Lett. **94**, 236 802 (2005)
4 T.D. Yuzvinsky, W. Mickelson, S. Aloni, S.L. Konsek, A.M. Fennimore, G.E. Begtrup, A. Kis, B.C. Regan, A. Zettl, Appl. Phys. Lett. **87**, 083 103 (2005)
5 K. Molhave, S.B. Gudnason, A.T. Pedersen, C.H. Clausen, A. Horsewell, P. Boggild, Nano Lett. **6**, 1663 (2006)
6 Y.H. Lee, J.H. Lee, S.J. Chung, S. Lee, B.K. Ju, Appl. Phys. Lett. **89**, 073 109 (2006)
7 S. Chen, J.Y. Huang, Z. Wang, K. Kempa, G. Chen, Z.F. Ren, Appl. Phys. Lett. **87**, 263 107 (2005)
8 J. Cumings, A. Zettl, Science **289**, 602 (2000)
9 A.N. Kolmogorov, V.H. Crespi, Phys. Rev. Lett. **85**, 4727 (2000)
10 M.F. Yu, B.I. Yakobson, R.S. Ruoff, J. Phys. Chem. B **104**, 8764 (2000)

11 A. Kis, K. Jensen, S. Aloni, W. Mickelson, A. Zettl, Phys. Rev. Lett. **97**, 025 501 (2006)
12 A.M. Fennimore, T.D. Yuzvinsky, W.Q. Han, M.S. Fuhrer, J. Cumings, A. Zettl, Nature **424**, 408 (2003)
13 B. Bourlon, D.C. Glattli, C. Miko, L. Forro, A. Bachtold, Nano Lett. **4**, 709 (2004)
14 L.X. Dong, B.J. Nelson, T. Fukuda, F. Arai, IEEE Trans. Autom. Sci. Eng. **3**, 228 (2006)
15 V.V. Deshpande, H.Y. Chiu, H.W.C. Postma, C. Miko, L. Forro, M. Bockrath, Nano Lett. **6**, 1092 (2006)
16 L. Maslov, Nanotechnology **17**, 2475 (2006)
17 Q.M. Yan, G. Zhou, S.G. Hao, J. Wu, W.H. Duan, Appl. Phys. Lett. **88**, 173 107 (2006)
18 K. Jensen, C. Girit, W. Mickelson, A. Zettl, Phys. Rev. Lett. **96**, 215 503 (2006)
19 J.W. Kang, K.O. Song, O.K. Kwon, H.J. Hwang, Nanotechnology **16**, 2670 (2005)
20 Q.S. Zheng, Q. Jiang, Phys. Rev. Lett. **88**, 045 503 (2002)
21 Q.S. Zheng, J.Z. Liu, Q. Jiang, Phys. Rev. B **65**, 245 409 (2002)
22 S.N. Lu, J. Chung J, R.S. Ruoff, Nanotechnology **16**, 1765 (2005)
23 A. Subramanian, B. Vikramaditya, L.X. Dong, D.J. Bell, B.J. Nelson, in *Robotics: Science and Systems I*, ed. by S. Thrun, G.S. Sukhatme, S. Schaal, O. Brock (MIT Press, 2005), p. 327
24 A. Bachtold, M.S. Fuhrer, S. Plyasunov, M. Forero, E.H. Anderson, A. Zettl, P.L. McEuen, Phys. Rev. Lett. **84**, 6082 (2000)
25 L. Shi, Mesoscopic thermophysical measurement of microstructures and carbon nanotubes, Dissertation, UC Berkeley (2001), p. 80
26 C. Yu, S. Saha, J. Zhou, L. Shi, A.M. Cassell, B.A. Cruden, Q. Ngo, J. Li, Trans. ASME **128**, 234 (2006)
27 T.Y. Choi, D. Poulikakos, J. Tharian, U. Sennhauser, Appl. Phys. Lett. **87**, 013 108 (2005)
28 T.Y. Choi, D. Poulikakos, J. Tharian, U. Sennhauser, Nano Lett. **6**, 1589 (2006)
29 T.W. Ebbesen, H.J. Lezec, H. Hiura, J.W. Bennett, H.F. Ghaemi, T. Thio, Nature **382**, 54 (1996)
30 H. Dai, E.W. Wong, C.M. Lieber, Science **272**, 523 (1996)
31 C. Berger, Y. YI, J. Gezo, P. Poncharai, W.A. de Heer, New J. Phys. **5**, 158 (2003)
32 B. Bourlon, D.C. Glattli, B. Placais, J.M. Berroir, C. Miko, L. Forro, A. Bachtold, Phys. Rev. Lett. **92**, 026 804 (2004)
33 M.A. Kuroda, A. Cangellaris, J.P. Leburton, Phys. Rev. Lett. **95**, 266 803 (2005)